Available online at www.sciencedirect.com
ScienceDirect
Earth and Planetary Science Letters 257 (2007) 14–28
EPSL
www.elsevier.com/locate/epsl

Teleseismic evidence for a break-off subducting slab under Eastern Turkey

Jianshe Lei [a,*], Dapeng Zhao [b]

[a] *Institute of Crustal Dynamics, China Earthquake Administration, Beijing 100085, China*
[b] *Geodynamics Research Center, Ehime University, Matsuyama 790-8577, Japan*

Received 30 October 2006; received in revised form 24 January 2007; accepted 4 February 2007
Available online 13 February 2007
Editor: G.D. Price

Abstract

We present seismic images of the upper mantle beneath Eastern Turkey determined by teleseismic tomography. The data are measured precisely from seismograms recoded by the Eastern Turkey Seismic Experiment network consisting of 29 portable stations and 2 permanent stations. Our results show that obvious high-velocity (high-V) anomalies of up to 2% are interrupted beneath Eastern Turkey, and subcrustal earthquakes occurred along these high-V anomalies. Pronounced low-velocity (low-V) anomalies are visible from the Arabian foreland basin in the southwest to the Caucasus region in the northeast, which extend down to about 400 km depth. These low-V anomalies are consistent with the existence of Late Cenozoic volcanism in the region. These results provide new constraints on the geodynamic processes in the east Anatolian plateau, suggesting that the break-off of the Arabian slab may play an important role in the formation of the Anatolian plateau and the volcanism in the region. These processes might be related to the collision of the Arabian plate with the Eurasian plate.

Keywords: subducted slab; break-off; geodynamic process; teleseismic tomography; Eastern Turkey

1. Introduction

Eastern Turkey is located at the intensely deformed Anatolian plateau, and its tectonic framework is dominated by the collision of the Arabian plate with Eurasia. In many aspects it can be thought of as a younger version of the Tibetan plateau [1–3]. The collision caused intense earthquake activity, widespread Pliocene to recent volcanism, strike-slip and thrust fault zones, and the westward escaped Anatolian plate. Late Cenozoic volcanism spreads widely from the Arabian foreland basin in the southwest to the Kars Plateau and Lesser Caucasus in the northeast. The dominated faults include Bitlis suture, the strike-slip north Anatolian fault [1,4,5], and the strike-slip east Anatolian fault [6,7] (Fig. 1). A wide variety of geophysical phenomena in the region raised particular interest in the complex evolution of the Anatolian plateau and surround regions.

Although many studies have been carried out to understand the geodynamic process of the Anatolian plateau, it is still a matter of debate. Some researchers suggested that the process was due to the Arabian plate convergence being accommodated entirely by microplate escape [1,7,8], or ascribed to the lithospheric

* Corresponding author. Tel.: +86 10 6295 8519; fax: +86 10 6292 7306.
E-mail addresses: leijs@eq-icd.cn (J. Lei), zhao@sci.ehime-u.ac.jp (D. Zhao).

0012-821X/$ - see front matter © 2007 Elsevier B.V. All rights reserved.
doi:10.1016/j.epsl.2007.02.011

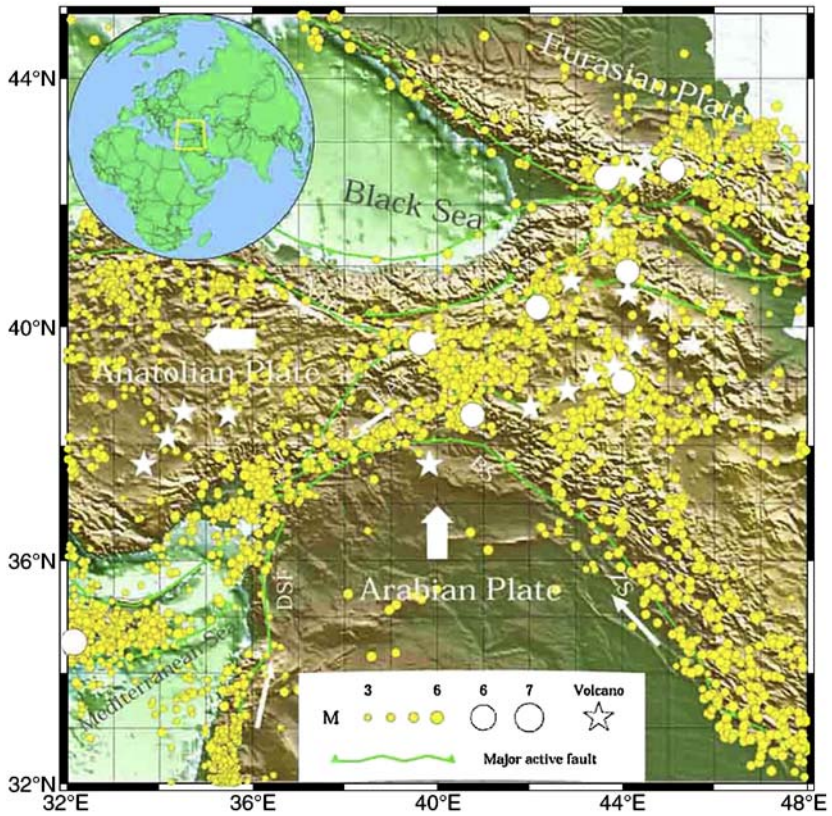

Fig. 1. Topographic map of the study area. Yellow and white circles denote the earthquakes with magnitudes smaller and greater than 6, respectively, during 1964–2003 reprocessed by Engdahl et al. [20]. White stars denote volcanoes. Plate boundaries and major faults are shown as green lines. NAF/EAF, North/East Anatolian Faults; BS, Bitlis Suture; DSF, Dead Sea Fault; ZS, Zagros Suture. Inserts show the location of the study area and ledge, respectively.

thickening [2], while others suggested that it was caused by the lithospheric delamination [9], or resulted from the continental subduction (e.g., [10]). There may be also a combination of these processes. Regional and global tomographic models obtained so far are still too rough to resolve the detailed and reliable structure under the region because of the sparseness of seismic stations deployed there and the relatively lower quality of the ISC (International Seismological Center) data set used.

With the recent installation of 29 portable seismic stations during the Eastern Turkey Seismic Experiment (ETSE) in 1999–2001 [11], several studies have been made to investigate the structure and understand the dynamic evolution of the Anatolian plateau. Sn attenuation models show that Sn waves were not observed in Eastern Turkey (e.g., [12]). Pn and Sn tomographic models show a prominent low-velocity (low-V) zone under the region [13–15]. Distribution of earthquake hypocenters with high accuracy shows no subcrustal earthquakes beneath the Arabian–Eurasian collision zone [16]. These studies indicated the presence of partial melts and absent mantle lid in Eastern Turkey and no or very little underthrusting of the Arabian plate beneath Eurasia. Fault plane solutions indicate the northward convergence of Arabia is being accommodated by escape tectonics [17]. P- and S-wave receiver-function studies displayed a normal-thickness crust, indicating that the crust may reside on an extremely thin mantle lithosphere, or perhaps directly on the asthenosphere [18,19]. However, no teleseismic tomography study has been made using this new data set. The availability of abundant teleseismic data recorded by the ETSE allows us to determine a detailed 3-D velocity structure beneath the region to understand the dynamic process forming the plateau.

In this study we have determined a 3-D P-wave velocity structure of the upper mantle beneath the region by applying an updated teleseismic tomogaphic technique to relative travel time residuals from the teleseismic events recorded by the portable seismic stations of the ETSE experiment, and two additional permanent broadband stations: GNI from the IU (Global

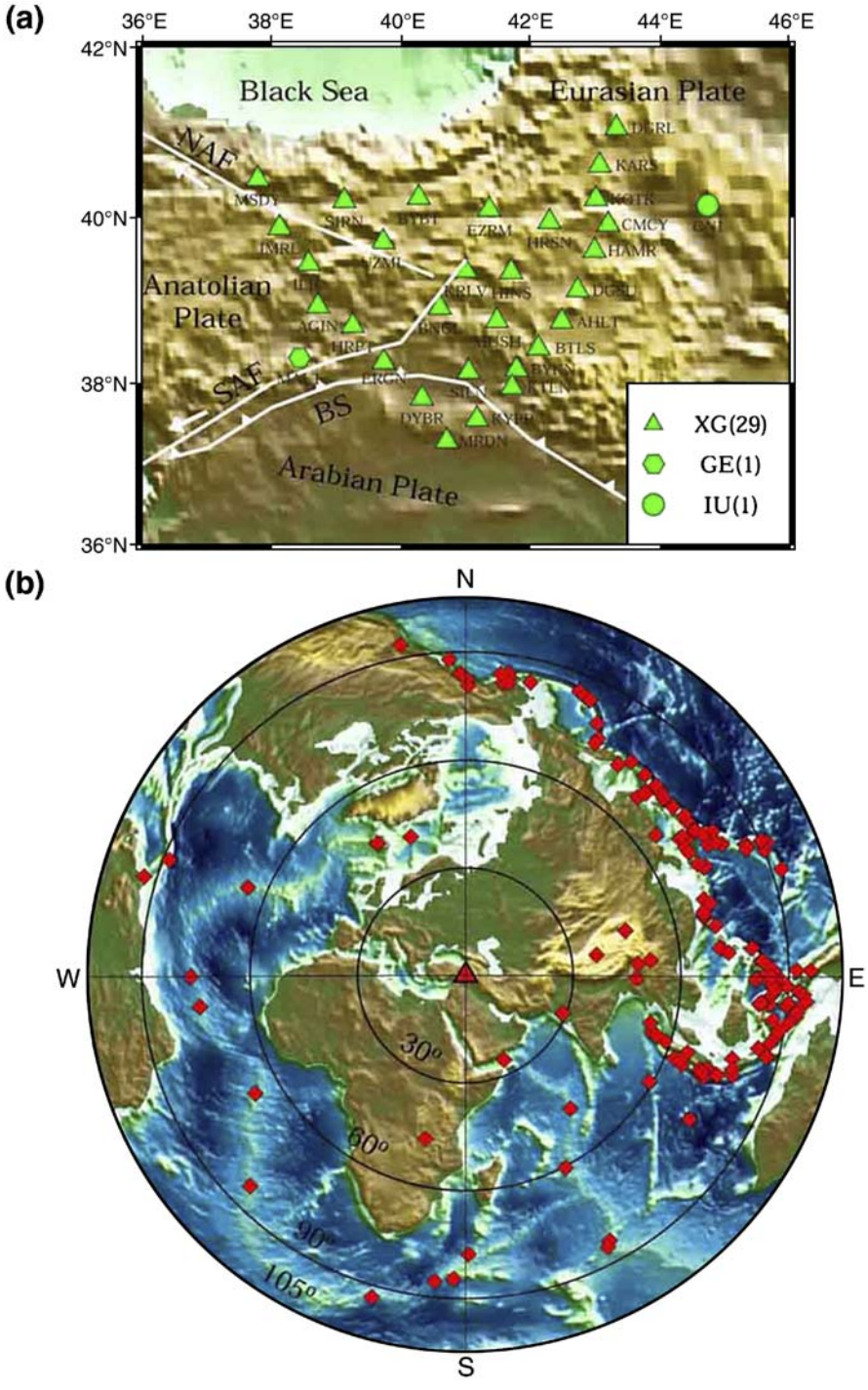

Fig. 2. (a) Distribution of the 31 seismic stations used in this study. Triangles denote the 29 PASSCAL broadband stations of the Eastern Turkey Seismic Experiment, the hexagon denotes the seismic stations from the GE network (GEOFON), and the circle represents the seismic station belonging to the IU (Global Seismograph Network, GSN-IRIS/USGS) network. White lines denote the plate boundaries and major faults. NAF/EAF denotes North/East Anatolian Faults. BS denotes Bitlis Suture. (b) Distribution of 190 teleseismic earthquakes (diamonds) used in this study. These hypocenters were reprocessed by Engdahl et al. [20]. The numbers represent the epicentral distances. The triangle denotes the center of the study area.

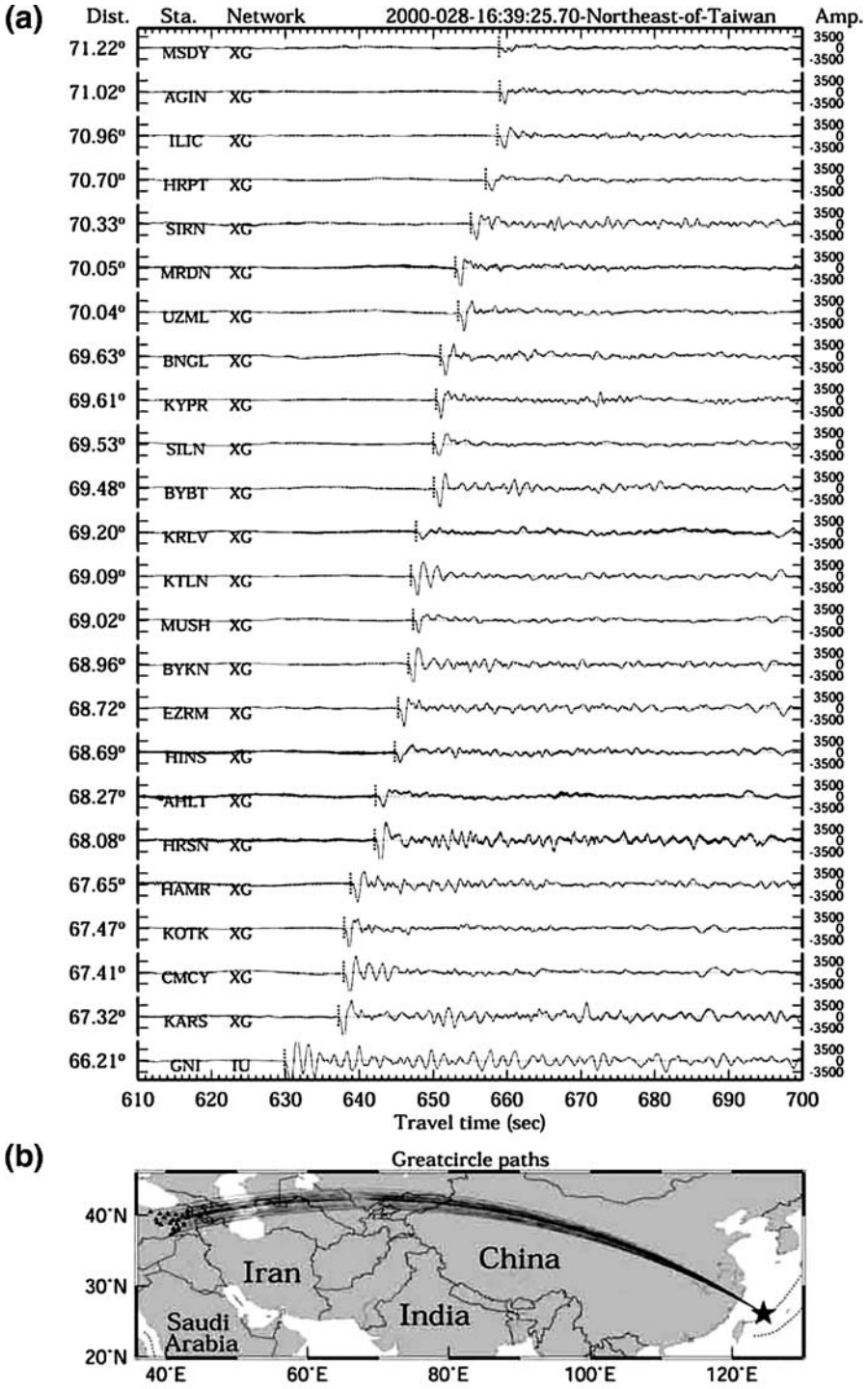

Fig. 3. (a) An example showing original vertical-component seismograms recorded by the Eastern Turkey Seismic Experiment and the IU network for an earthquake with a magnitude of Mw 6.0 occurred in the Northeast of Taiwan on January 28, 2000. The vertical dashed lines show the P first arrivals we picked using the multi-channel cross-correlation technique of VanDecar and Crosson [21]. The letters on the left denote the seismic stations and networks, respectively. The number on the left denotes the epicentral distance in degree. (b) Great circle paths for the traces in (a). The star and triangles denote the epicenter and seismic stations deployed in Eastern Turkey, respectively.

Seismograph Network, GSN-IRIS/USGS) network, and MALT from the GE (GEOFON Network, GFZ-Potsdam) network. Our tomographic results shed new light on the dynamic processes of the Anatolian plateau.

2. Data and method

Fig. 2a shows the distribution of 31 seismic stations used in this study. Among them, the 29 portable broadband seismic stations of the ETSE network were deployed by scientists from both Bogazici University, Kandilli Observatory in Turkey and Cornell University in U.S.A. These stations were all equipped with broadband three-component STS-2 sensors except for one Guralp CMG-3T sensor at station EZRM, and were operated for a period of 22 months from November 1999 to July 2001. The portable network traversed several regions with different tectonic features: the Arabian plate, the east Anatolian plateau, the Bitlis suture, the east Anatolian fault, and the north Anatolian fault. In this work, we also added two permanent seismic stations, MALT and GNI, which were selected from the GE and IU networks, respectively. These two permanent stations are very close to the portable seismic network (see Fig. 2a).

The 190 teleseismic events we selected (Fig. 2b) were recorded by the seismic stations as mentioned above. Each event has at least 8 recordings. We used their hypocenter parameters determined by Dr. E.R. Engdahl with a procedure described in Engdahl et al. [20]. The magnitude of these events is greater than M 4.8. The events selected have a good azimuthal coverage, and have an epicentral distance between 28° and 96° from the center of the network. We picked first P-wave travel times from the high-quality original seismograms (Fig. 3) by using the multi-channel cross-correlation technique of VanDecar and Crosson [21]. The picking accuracy is estimated to be 0.1–0.15 s. The

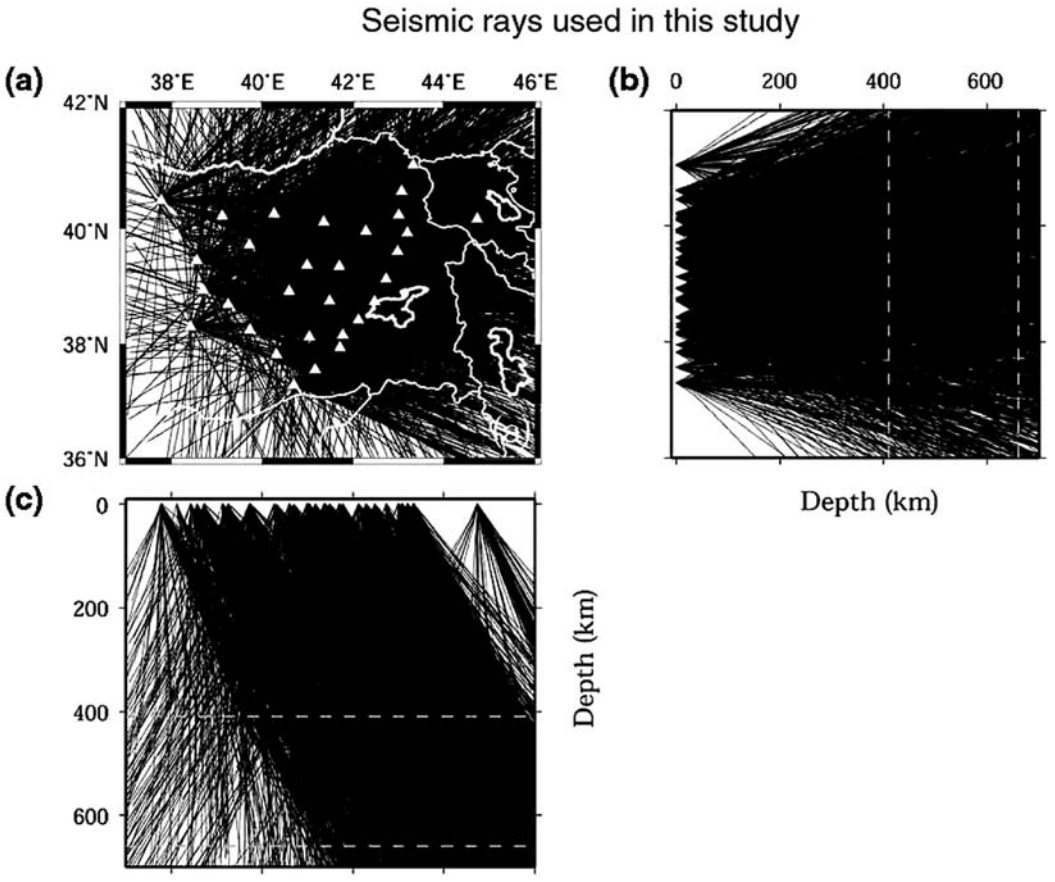

Fig. 4. Distribution of P-wave ray paths used in this study in map view (a) and in the north–south (b) and east–west (c) vertical cross-sections. White triangles denote the seismic stations used in this study. White curves represent the boundary of countries.

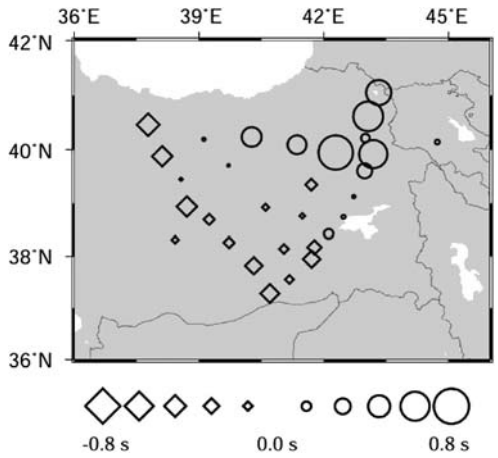

Fig. 5. Distribution of relative travel time residuals at each of the 31 seismic stations. Diamonds and circles denote negative and positive residuals, respectively. The scale for the residuals (in s) is shown at the bottom.

resulting data set contains over 3900 high-quality P arrivals. The seismic rays used in this study are shown in Fig. 4.

An updated version of the 3-D ray tracer of Zhao [22] is used to compute the theoretical travel times. They are corrected for the Earth's ellipticity [23]. The station elevations are taken into account in the 3-D ray tracing. When calculating the travel times, we also determined the teleseismic ray paths between the hypocenter and receiver and found the intersection between the ray and the boundary plane of the modeling space. Then we determined the ray path between the intersection and the station. This 3-D ray tracer can compute the travel times and ray paths efficiently and accurately, and can deal with a velocity model that contains velocity discontinuities of complex geometry and 3-D velocity variation everywhere in the model. For details, see Zhao et al. [24] and Zhao and Lei [25].

In order to minimize the effects of the uncertainties in hypocenter locations and original times, as well as the velocity heterogeneity outside the study area, we used the relative travel time residuals in the tomgoraphic inversion. For details of the calculation of the relative residuals, see Zhao et al. [26] and Lei and Zhao [27,28]. Fig. 5 shows the distribution of the average relative travel time residuals at each station, which shows a clear pattern of delayed and early arrivals. The maximum amplitude of early and delayed arrivals amounts to 0.8 s. Delayed arrivals are visible at stations around the Neogene/Quaternary volcanoes east and north of the triple Karliova junction, where low-V anomalies may exist in the upper mantle, while early arrivals appear at stations in the north of the Arabian plate and west and south of the triple Karliova junction, where high-V anomalies may exist in the upper mantle.

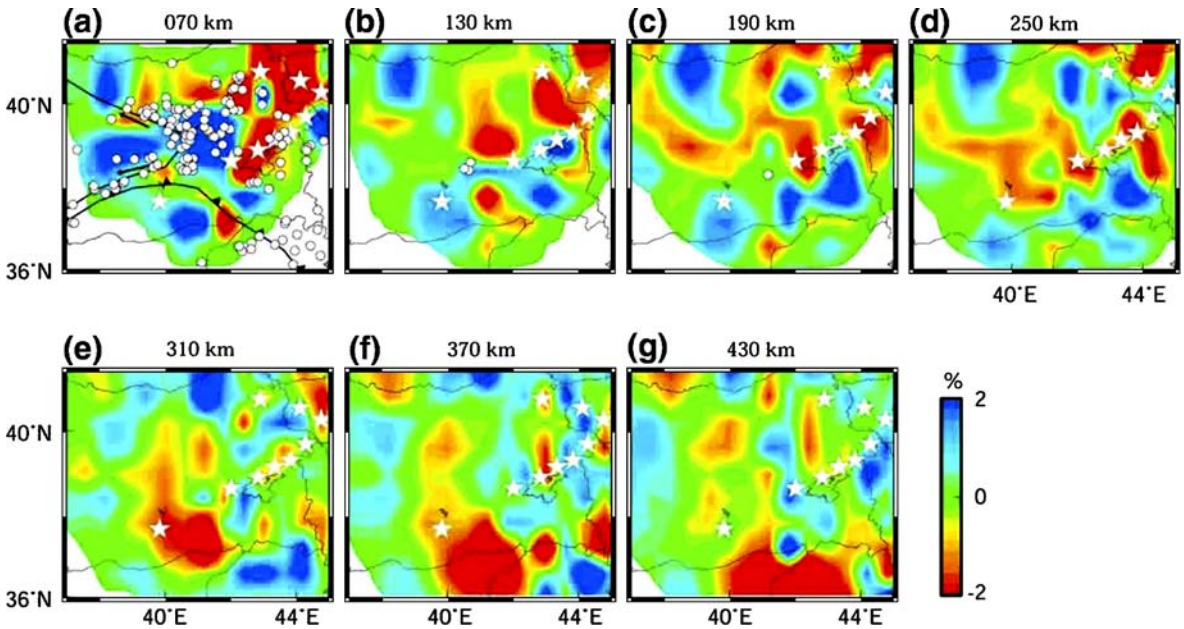

Fig. 6. Tomographic images in map view obtained after the crustal correction using the model of Zor et al. [18], based on the iasp91 Earth model [50]. Red and blue colors denote slow and fast velocity anomalies, respectively. The scale for the velocity perturbation (in %) is shown on the right of (g). The layer depth is shown above each map. White stars denote the volcanoes. White circles in (a)–(c) denote the earthquakes occurred within a range of 30 km above and blow the layer depth. Thick black lines denote the plate boundaries and major faults.

We applied the tomographic method of Zhao et al. [26] to the relative travel time residuals for determining the 3-D velocity structure beneath Eastern Turkey. A 3-D grid was set up in the model and velocity perturbations at the grid nodes were taken as unknown parameters. The grid spacing of the model is $0.6° \times 0.6°$ laterally and 60 km in depth. The velocity perturbation at any point in the model was obtained by interpolating the velocity perturbations at the eight grid nodes surrounding that point. A conjugate gradient algorithm [29] with damping and smoothing [22,30] was used to invert the large and spare system of observation equations.

3. Results and resolution analyses

Teleseismic rays do not crisscross well in the shallow crust, and so the crustal structure cannot be resolved well, which is usual for teleseismic tomography. The teleseismic tomography result is usually corrected for the crustal heterogeneity (e.g., [27,28,31,32]). Lei and Zhao [28] discussed the influence of different crustal models on the mantle image, and found that a detailed crustal structure is required for the teleseismic tomography. In this study we performed the corrections for the crustal heterogeneity by adopting the crustal model of Zor et al.

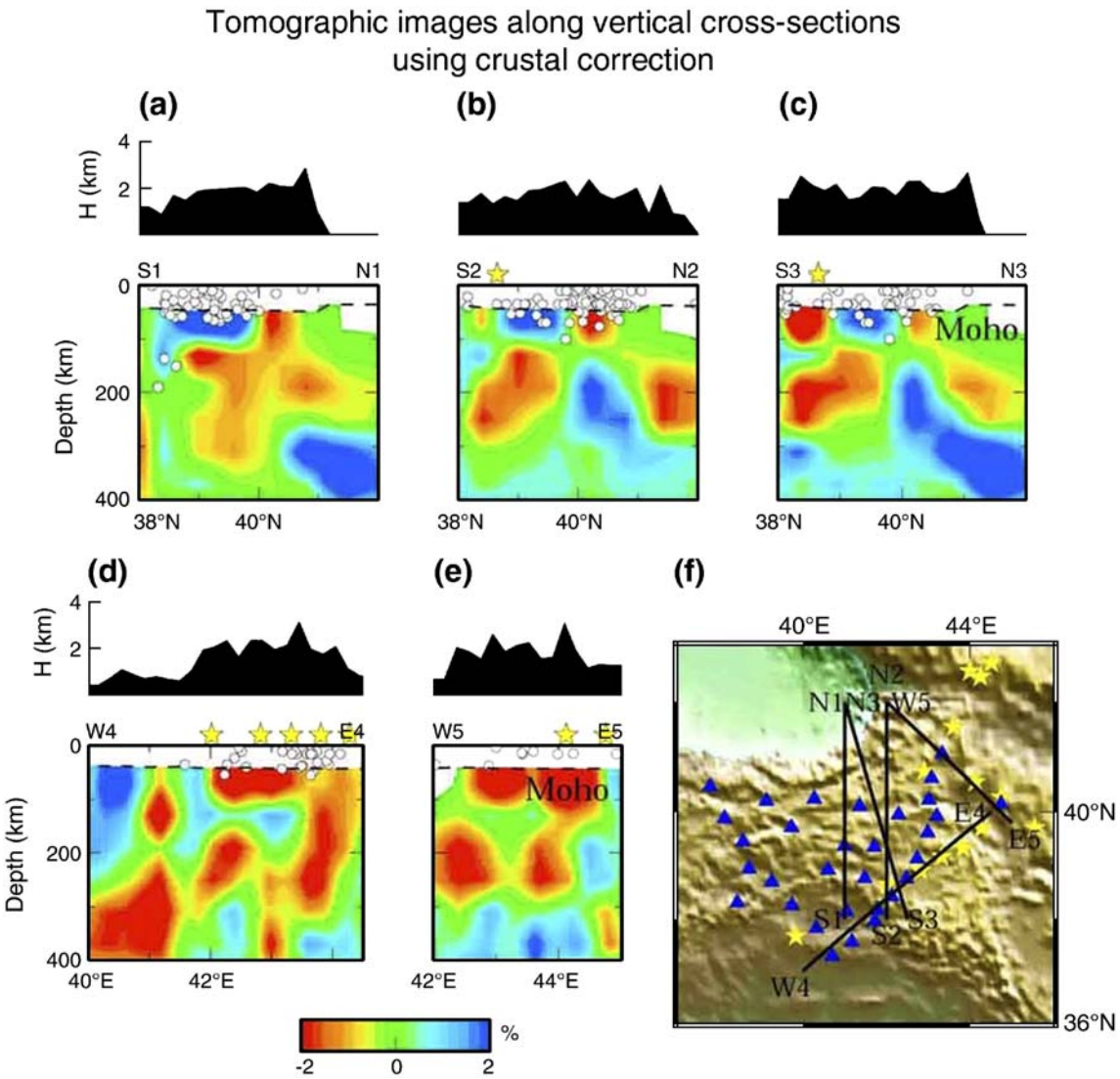

Fig. 7. (a)–(e) The same as Fig. 6 but for the vertical cross-sections as shown in (f). Red and blue colors denote slow and fast velocity anomalies, respectively. The scale for the velocity perturbation (in %) is shown at the bottom. Circles in (a)–(e) denote the earthquakes occurred within 30 km off the profile. Stars in (a)–(f) denote the volcanoes. The polygons above each map denote the topography along the cross-section. Triangles denote the seismic stations.

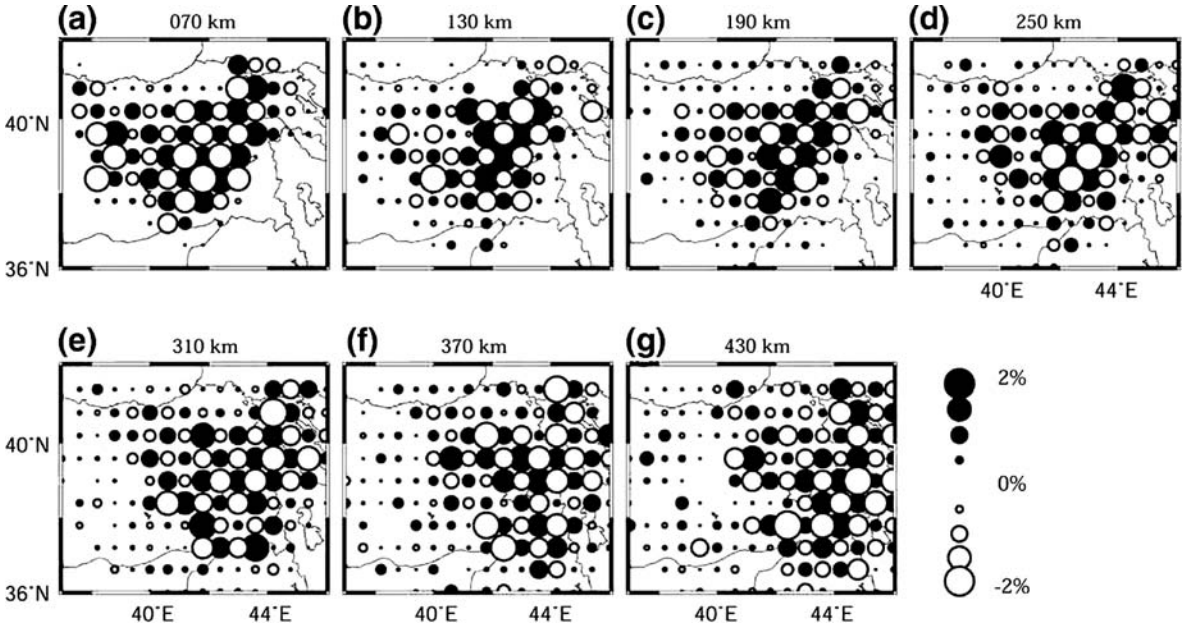

Fig. 8. Results of a checkerboard resolution test for P-wave structure in map view. The model is parameterized with a grid spacing of 0.6° × 0.6° × 60 km. The layer depth is shown above each map. Open and solid circles denote slow and fast velocity anomalies, respectively. The scale for the velocity perturbation (in %) is shown on the right of (g).

[18] for the region. This crustal model contains both lateral velocity variations in the crust and depth variations of the Moho discontinuity, which is inferred from the receiver function technique. For details, see Zor et al. [18].

Fig. 6 shows our final tomographic images in map view. In the shallower mantle striking high-V anomalies are visible north of the north Anatolian fault, in the north Arabian plate, and around the triple Karliova junction

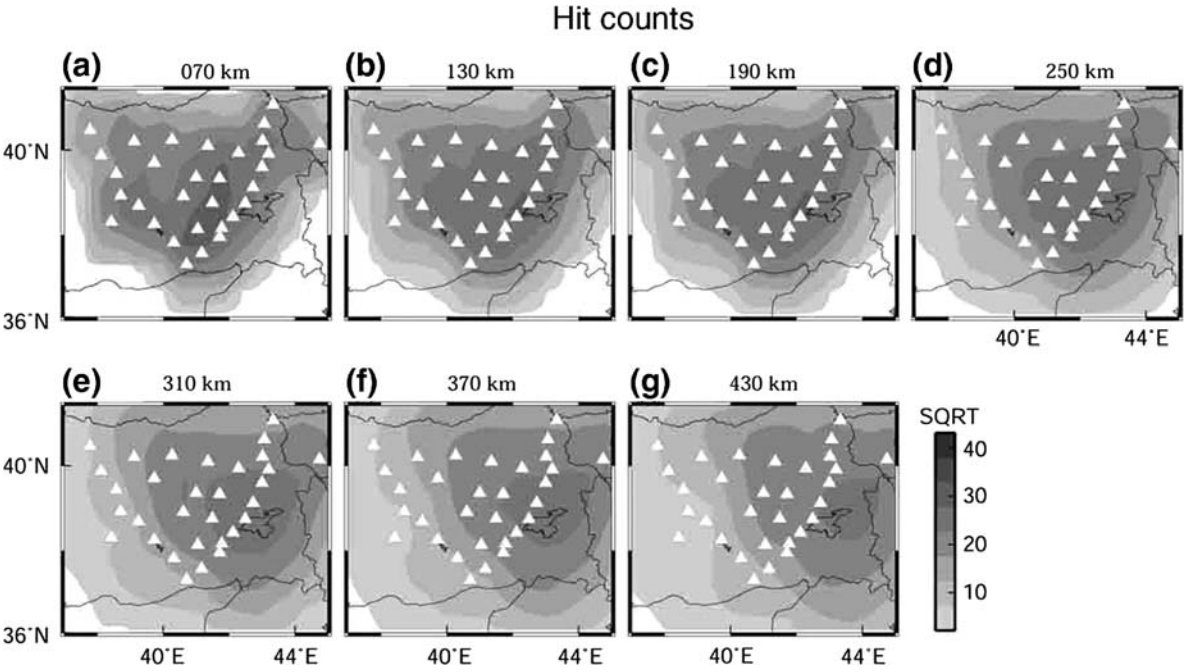

Fig. 9. Distribution of the number of the rays passing through each grid node (hit counts) in map view. The layer depth is shown above each map. The scale for hit counts in the square root (SQRT) is shown on the right of (g). The triangles denote the seismic stations used in this study.

from the west to the east. These high-V anomalies are separated by weak low-V anomalies along the east Anatolian fault, the north Anatolian fault, and the Bitlis suture (Fig. 6a). This may be related to the westward movement of the Anatolian plate and the subduction of the Arabian plate. Most of earthquakes occurred in and around the high-V anomalies. A zone of broad low-V anomalies is observed east of the triple Karliova junction and in the Caucasus region, which is consistent with the distribution of the Quaternary volcanoes within the east Anatolian plateau. At 130 km depth high-V anomalies north of the north Anatolian plate and in the Arabian plate extend down to 250 km depth (Figs. 6b–d). At these depths some obvious low-V anomalies are also revealed in the central portion of the studying area. These low-V anomalies extend down toward beneath the Arabian plate (Figs. 6e–g), suggesting that the volcanoes may originate from the mantle transition zone or deeper.

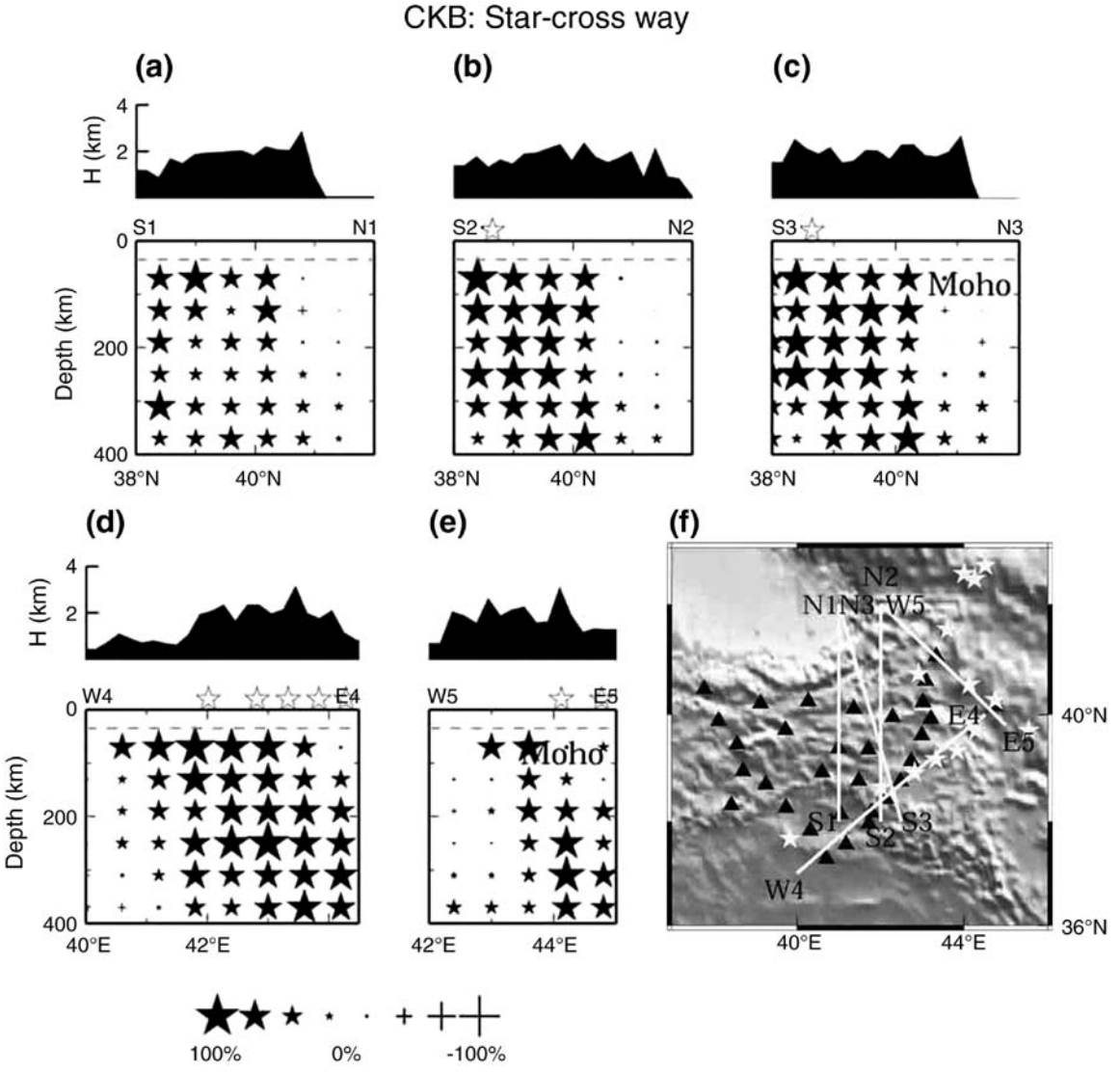

Fig. 10. (a)–(e) Results of the checkerboard resolution test for P-wave structure along the vertical cross-sections. The star-cross way is used to express the resolution because some of cross-sections, such as N3–S3, W4–E4, and W5–E5, are not just passing through the grid nodes of the model. Solid stars denote the grid nodes where the pattern of the input velocity anomalies is retrieved correctly after the inversion, while crosses denote the grid nodes where the pattern of the input velocity anomalies is wrongly recovered after the inversion. The scale for the degree of recovery (in %) is shown at the bottom. For details, see Lei and Zhou [34], Lei and Zhao [27,28]. The dashed line denotes the Moho discontinuity. The polygons above each map denote the topography along the cross-section. (f) Location of the vertical cross-sections. Triangles denote the seismic stations. Open stars in (a)–(f) denote the volcanoes.

Around the Caucasus region an obvious high-V anomaly is imaged at depths of 190–370 km, which may present the break-off slab (Figs. 6c–f).

Fig. 7 illustrates our final tomographic images along several vertical cross-sections. The Arabian subducting slab is clearly imaged as high-V anomalies which are intermittent at about 100 km depth from the center to the east of the study area (Fig. 7a–c). Moreover, the larger break-off occurred in the center (Fig. 7a). Some low-V anomalies are visible above and below the subducting slab (Fig. 7a–c). In the central portion the low-V anomalies below the slab are connected to those above the slab through the slab break-off (Fig. 7a). Low-V anomalies below the slab ascend upward to the surface (Fig. 6c), which may be related to the Arabian foreland volcanism. Low-V anomalies above the slab reach the surface (Figs. 7a–c), which may be associated with the volcanism within the east Anatolian plate. In Fig. 6d and e it can be seen that some prominent low-V anomalies beneath the volcanoes extend down to 400 km depth from the surface.

In order to evaluate the resolvability of our data set and to confirm the main features of our tomographic image, we conducted two kinds of the resolution tests (e.g., [26–28,33]). One is the checkerboard resolution test for examining the spatial resolution of our tomographic image in the entire study area. The other is the restoring test for evaluating the main features presented in our result. Random noises with zero mean and a standard deviation of 0.1 s were added to the

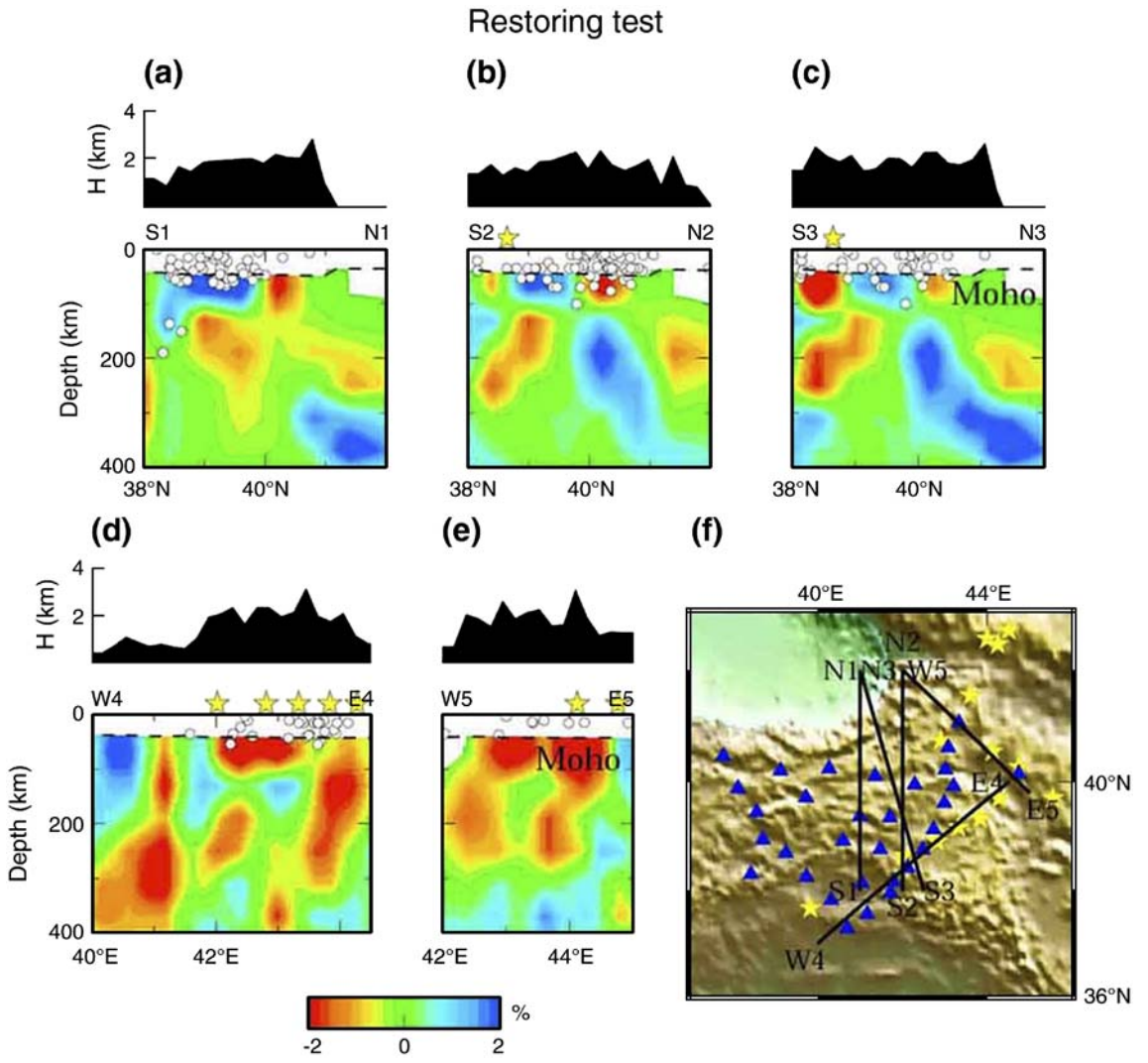

Fig. 11. Output model of a restoring test using the same inversion technique and the same data set with the Gaussian noise. Input model is the tomographic images obtained as shown in Fig. 7. The other symbols are the same as in Fig. 7.

synthetic travel times to account for data errors which are usually present in a real data set. The model has been parameterized with an optimal grid spacing of 0.6°×0.6° laterally and 60 km vertically after making many resolution tests with different grid spacing. The difference between them is just in the input model. In the checkerboard resolution test, positive and negative 2% velocity perturbations are assigned to 3-D grid nodes that are arranged in the modeling space. In the restoring test the images obtained from the real inversion (Figs. 6and 7) are taken as our input model.

The resolution is good for the area covered by the stations from 70 to 190 km depth (Fig. 8a–c). From 250 to 430 km depth the good-resolution areas eventually bias toward the east (Fig. 8d–g) because more earthquakes (Fig. 2b) and ray paths (Fig. 4a and c) are distributed in the east. The distribution of hit counts also shows such a feature (Fig. 9). To clearly see whether the main features of our image are reliable, the results of the checkerboard resolution test along vertical cross-sections are illustrated (Fig. 10) using the star-cross way through which it is easy and straightforward to understand where the resolution is good and where it is poor (e.g., [27,28,34]). The resolution is good around and below the subducting slab, and it is relatively poor above the subducting slab (Fig. 10a–c). Along the cross-section of W4-E4, the resolution is good in the entire segment except for a small area at the bottom of the western end (Fig. 10d). Along the cross-section of W5-E5, the resolution is much better in the east segment than that in the west segment (Fig. 10e).

From the restoring test (Fig. 11) it can be seen that though the amplitude of velocity anomalies are not completely retrieved, their pattern is fully recovered as shown in the real inversion (Fig. 7). There is some vertical smearing in the west segment of W5-E5 (Fig. 11e), which is in agreement with the poor resolution as shown in Fig. 10e. These extensive resolution tests all demonstrate that the main features of our present results are reliable.

4. Discussion

The upper mantle P-wave velocity structure deduced from the teleseismic tomography provides insight into the dynamic processes of the upper mantle beneath the region. Pronounced high-V anomalies are observed beneath the Bitlis suture from the Moho depth to 400 km depth. Some intermediate-depth (around 100 km) earthquakes form a clear Wadati–Benioff zone along the high-V anomaly zone (Fig. 7). These results suggest the existence of the subducted Arabian slab under Eastern Turkey, which is consistent with the results from the surface-wave tomography of Maggi and Priestley [35] and the regional body-wave tomography of Piromallo and Morelli [36]. An earlier work of Rotstein and Kafka [10] also indicated the existence of the subducting Arabian slab beneath the Anatolian plate through displaying earthquakes present beneath the crust, though recent studies show the absence of sub-crustal earthquakes after accurate hypocenter relocation (e.g., [16]), perhaps due to the short-term recording of earthquakes.

One of the significant tectonic features in our present velocity model is the separation of the high-V anomalies around 100 km depth along the slab (Fig. 7). This separation may denote the break-off of the subducted Arabian slab. Davies and von Blanckenburg [37] also suggested a similar depth value for the slab break-off under the east Anatolian plateau. The slab break-off means the detachment of oceanic lithosphere from the continental lithosphere during the continent-continent collision, which helps to explain many of the observations in collision zones. Such a tectonic feature is also revealed in the Tien Shan region (e.g., [28]), the Pamir region (e.g., [38]), and the Tertary Eurapean Alps and the Aegean (e.g., [39]). Faccenna et al. [40] displayed the absence of the high-V anomalies around 100 km depth in the model of Piromallo and Morelli [36] derived from the inversion of ISC (1964–1995) P-wave delay times. However, there is still some difference between our model and the model of Piromallo and Morelli [36]. The model of Piromallo and Morelli [36] shows that the high-V anomalies are totally lost above 200 km depth, while a prominent high-V anomaly above 100 km depth still exists in our model (Fig. 7), which is consistent with the result from surface wave tomography showing a high-V anomaly extending down to 100 km depth beneath the Arabian shield [35]. Such difference may be due, in part, to the high quality and good ray coverage of the data set used in the present study. In addition, the slab break-off is different in size from the east to the west, which may be caused by the differential moving rate (about 10–25 mm/yr) between the Arabian and African plates [5]. Such a break-off difference is also observed in the Mediterranean–Carpathian region [39].

Pronounced and extensive low-V anomalies beneath Eastern Turkey are also visible in the present result (Figs. 6 and 7). This is consistent with the results from Pn tomography [13–15], Sn tomography [12,15], and surface waveform tomography [35]. Sn attenuation studies show that Sn waves are strongly attenuated for propagation paths across this region [12,41]. High gravity anomalies [42] and shallow Curie-point depths [43] are also revealed beneath the region. A high heat-flow

distribution shows a similar feature [44]. Orgulu et al. [17] observed that the crustal stress field has changed dramatically in the past 5 to 10 Ma. These observations suggest that the uppermost mantle is partially molten and the asthenosphere is close to the base of the crust, consistent with the existence of the volcanism in the region (Fig. 1). The volcanism in Eastern Turkey has been active since the Late Miocene, which may be ascribed in part to the subducted Tethyan oceanic lithosphere beneath Eurasia [13,14].

Another significant tectonic feature in our present work is the existence of low-V anomalies beneath and above the subducted slab in the Turkey region (Fig. 7). Such a feature is quite similar to that in the northwest Pacific region (e.g., [26,30,45]). Low-V anomalies above the slab are in agreement with the distribution of active arc volcanoes in the Japan islands caused by the dehydration of the subducting Pacific and Philippine Sea slabs. However, low-V anomalies under the slab are different in morphology in these two regions. Low-V anomalies under the Pacific slab did not reach the surface in the Pacific region. The causes of these low-V anomalies beneath the slab are still unclear, but there are two possibilities: One is that they present a hot upwelling portion of a local-scale convection associated with the subduction of the Pacific slab; the other is that they show a small mantle plume rising from the lower mantle [45]. Low-V anomalies under the slab in the Turkey region are divided into two branches. One is that they are connected to the low-V anomalies above the slab by going through the break-off of the subducted Arabian slab. The other is that they ascend directly to the surface along the lower boundary of the Arabian slab, which may be related to the Arabian foreland volcanism. The results from geochemical studies suggested that the foreland volcanism is dominated by basaltic shield and fissure eruptions of transitional tholeiitic-alkaline composition [9,46]. Isotope and trace element analyses suggested that the lavas from the foreland were derived from the mantle lithosphere of the Arabian continent,

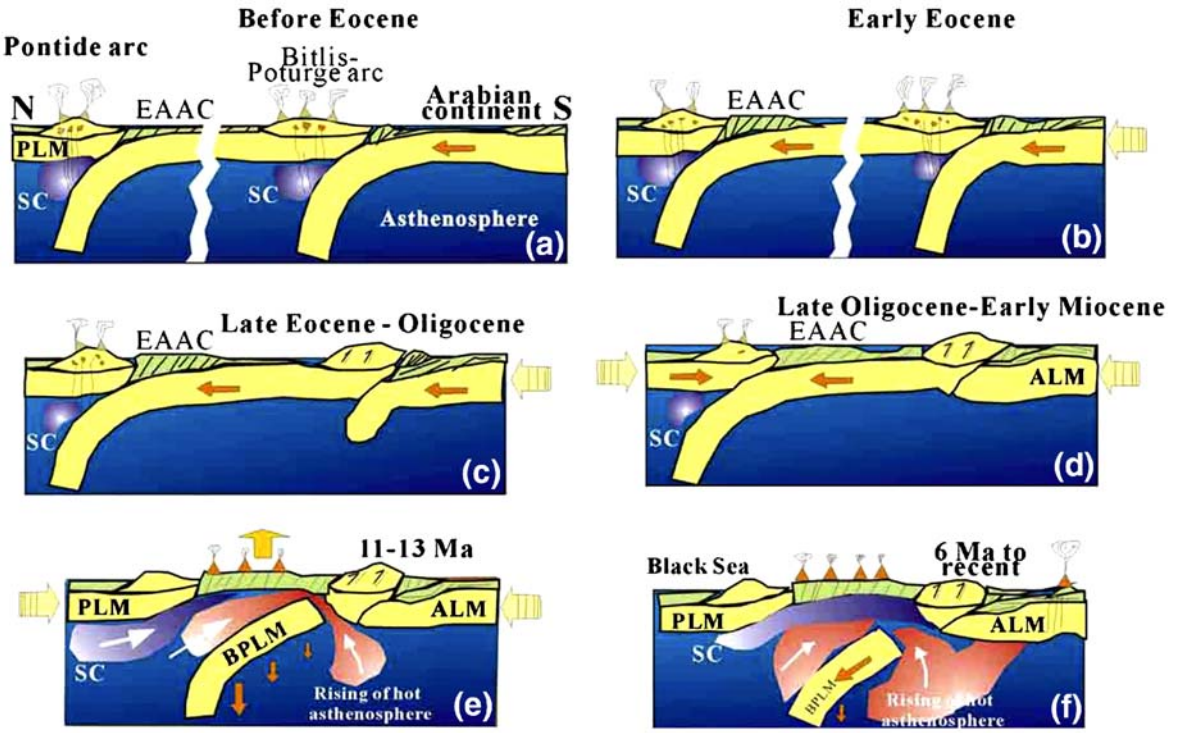

Fig. 12. Cartoons displaying regional uplift and magma generation caused by the slab break-off in Eastern Anatolia. (a)–(b) The oceanic realm was open and the Neo-Tethys Arabian oceanic slab was subducting before Early Eocene; (c) The oceanic realm was closed between Late Eocene and Oligocene, when the EAAC made its initial contact with the Bitlis–Porurge Massif; (d) The EAAC was shortened and thickened over the oceanic lithenospheric slab between Late Oligocene and 13–15 Ma; (e) The slab was possibly steepened and eventually detached from the EAAC during around 11–13 Ma, due to the buoyancy contrast between the slab and the Bitlis–Porurge Massif; (f) The break-off slab still exists in the asthenosphere during 6 Ma to the present, which is different from the models of Sengor et al. [47] and Keskin [48] proposing the disappearance of the break-off slab. SC, asthenospheric mantle containing a subduction component; SSF, Strike-slip faults; PLM, lithospheric mantle of the Pontides; BPLM, lithospheric mantle of the Bitlis–Poturge Massif; ALM, Arabian lithospheric mantle.

which had previously been enriched by small volumes of asthenospheric melts, and lavas from the alkaline volcanics north of the Bitlis suture zone were derived from a lithospheric source of a similar composition. The transitional and calc-alkaline lavas from the northernmost volcanics appear to be derived from the lithosphere having a subduction signature inherited from pre-collision subduction events.

Surface wave tomographic studies show that a pronounced low-V anomaly beneath the volcanoes in Eastern Turkey is extending down to only around 200 km depth, which may be due to its low-resolution model under 200 km depth [35]. However, our present results display significant low-V anomalies beneath the volcanoes extending down to around 400 km depth under the Arabian plate (Figs. 6 and 7d), which may be associated with a small-scale mantle plume. This tectonic feature has been demonstrated to be reliable through extensive synthetic and checkerboard resolution tests (Figs. 8, 10 and 11).

Davies and von Blanckenburg [37] once suggested a slab break-off model allowing the explanation of syn- to post-collisional magmatism and metamorphism. Sengor et al. [47] and Keskin [48] modified the model of Davies and von Blanckenburg [37], indicating a large accretionary prism precluding the opposition of two converging continents, and under which a slab gradually gets steepened until it is finally detached. Hence the previous work and the present study all suggest the following dynamic processes for the formation of the Anatolian plateau and its geophysical phenomenon. The oceanic realm in the region was closed in a period between Late Eocene and Oligocene when the Eastern Anatolian Accretionary Complex (EAAC) made its initial contact with the Bitlis–Porurge Massif (Fig. 12c). During the period between Late Oligocene and 13–15 Ma, the EAAC was shortened and thickened over the oceanic lithospheric slab (Fig. 12d), until the slab was possibly steepened and eventually detached from the EAAC around 10–11 Ma (Fig. 12e), due to the buoyancy contrast between the slab and the Bitlis–Porurge Massif. This model involves the break-off of a northward subducted slab that allowed hot, partially molten asthenospheric material to be in close proximity to the bottom of the crust. This could explain the initiation of collisional volcanism and the relatively rapid regional uplift to form the 2 km high Anatolian plateau. However, there also exists some difference between our present model and the models of Sengor et al. [47] and Keskin [48]. The model of Sengor et al. [47] and Keskin [48] indicated the disappearance of the break-off slab in the asthenosphere finally, while our present model emphasizes the current existence of the break-off slab in the asthenosphere (Fig. 12f), which may play an important role in the formation of the widespread volcanism within Anatolia and in the dynamically supported uplift of the east Anatolian plateau.

5. Conclusions

A high-resolution tomographic model under Eastern Turkey is obtained by applying an updated teleseismic tomographic technique to a large number of arrival time data recorded by the portable seismic stations from the ETSE experiment and two permanent stations. Our present results provide new constraints on the geodynamic process of the Anatolian plateau. The subducted Arabian slab has been clearly broken-off under the Anatolian plateau, which might play an important role in the formation of the volcanism and in the uplift of the Anatolian plateau. These processes may be associated with the collision of the Arabian plate with the Eurasian plate.

Acknowledgements

We thank the IRIS Data Management Center for providing the waveform data used in this study. R. Engdahl provided the hypocentral parameters of the teleseismic events he relocated. We are grateful to T. Hirano for his assistance at the data processing stage, to Y. Ai for thoughtful discussion. This work was partially supported by Development Foundation of Science and Technology from ICD (200604) to J. Lei and a research grant (Kiban-A 17204037) from the Japanese Ministry of Education and Science to D. Zhao. The GMT software package distributed by Wessel and Smith [49] was used for plotting the figures. Prof. G.D. Price and an anonymous reviewer provided constructive comments and suggestions, which improved the manuscript.

References

[1] A. Sengor, W. Kidd, Post-collisional tectonics of Turkish–Iranian Plateau and a comparison with Tibet, Tectonophysics 55 (1979) 361–376.

[2] J. Dewey, M. Hempton, W. Kidd, Z. Saroglu, A. Sengor, Shortening of continental lithosphere: the neotectonics of eastern Anatolian—a young collision zone, in: M. Coward, A. Ries (Eds.), Collosion Tectonics, Geological Society Special Publications, vol. 19, 1986, pp. 3–36.

[3] M. Barazangi, Continental collision zones: seismotectonics and crustal structure, in: D. James (Ed.), Encyclopedia of Solid Earth Geophysics, Nostrand, Reinhold Company, New York, 1989, pp. 58–75.

[4] J. Dewey, A. Sengor, Aegean and surroundings regions: complex multiplate and continuum tectonics in a convergent zone, Geol. Soc. Amer. Bull. 90 (1979) 84–92.

[5] S. McClusky, S. Balassanian, A. Barka, C. Demir, S. Ergintav, I. Georgiev, O. Gurkan, M. Hamburger, K. Hurst, H. Kahle, K. Kastens, G. Kekelidze, R. King, V. Kotzev, O. Lenk, S. Mahmoud, A. Mishin, M. Nadariya, A. Ouzounis, S. Paradissis, Y. Peter, M. Prilepin, R. Reilinger, I. Sanli, H. Seeger, A. Tealeb, M. Toksoz, G. Veis, GPS constraints on plate motion and deformation in the eastern Mediterranean: implications for plate dynamics, J. Geophys. Res. 105 (2000) 5695–5719.

[6] D. McKenzie, Active tectonics of the Mediterranean region, Geophys. J. R. Astron. Soc. 30 (2) (1972) 109–185.

[7] J. Jackson, D. Mckenzie, The relationship between plate motions and seismic moment tensors, and the rates of active deformation in the Mediterranean and Middle East, Geophys. J. Int. 93 (1988) 45–73.

[8] D. McKenzie, The East Anatolian Fault: a major structure in eastern Turkey, Earth Planet. Sci. Lett. 29 (1976) 109–185.

[9] J. Pearce, J. Bender, S. De Long, W. Kidd, P. Low, Y. Guner, F. Saroglu, Y. Yilmaz, S. Moorbath, J. Mitchell, Genesis of collision volcanism in Eastern Anatolia, Turkey, J. Volcanol. Geotherm. Res. 44 (1990) 189–229.

[10] Y. Rotstein, A. Kafka, Seismotectonics of the southern boundary of Anatolia, eastern Mediterranean region: subduction, collision, and arc jumping, J. Geophys. Res. 87 (1982) 7694–7706.

[11] E. Sandvol, N. Turkelli, M. Barazangi, The Eastern Turkey Seismic Experiment: the study of a young continent–continent collision, Geophys. Res. Lett. 30 (2003), doi:10.1029/2003GL018912.

[12] R. Gok, E. Sandvol, N. Turkelli, D. Seber, M. Barazangi, Sn attenuation in the Anatolian and Iranian plateau and surrounding regions, Geophys. Res. Lett. 30 (2003), doi:10.1029/2003GL018020.

[13] A. Al-Lazki, D. Seber, E. Sandvol, N. Turkelli, R. Mohamad, M. Barazangi, Tomographic Pn velocity and anisotropy structure beneath the Anatolian plateau (eastern Turkey) and surrounding regions, Geophys. Res. Lett. 30 (2003), doi:10.1029/2003GL017391.

[14] A. Al-Lazki, E. Sandvol, D. Seber, M. Barazangi, N. Turkelli, R. Mohamad, Pn tomographic imaging of mantle lid velocity and anisotropy at the junction of the Arabian, Eurasian and African plates, Geophys. J. Int. 158 (2004) 1024–1041.

[15] K. Al-Damegh, E. Sandvol, A. Al-Lazki, M. Barazangi, Regional seismic wave propagation (Lg and Sn) and Pn attenuation in the Arabian plateau and surrounding regions, Geophys. J. Int. 157 (2004) 775–795.

[16] N. Turkelli, E. Sandvol, E. Zor, R. Gok, T. Bekler, A. Al-Lazki, H. Karabulut, S. Kuleli, T. Eken, C. Gurbuz, S. Bayraktutan, D. Sber, M. Barazangi, Seismogenic zones in Eastern Turkey, Geophys. Res. Lett. 30 (2003), doi:10.1029/2003GL018023.

[17] G. Orgulu, M. Aktar, N. Turkelli, E. Sandvol, M. Barazangi, Contribution to the seismotectonics of Eastern Turkey from moderate and small size events, Geophys. Res. Lett. 30 (2003), doi:10.1029/2003GL018258.

[18] E. Zor, E. Sandvol, C. Gurbuz, N. Turkelli, D. Seber, M. Barazangi, The crustal structure of the Eastern Anatolian plateau (Turkey) from receiver functions, Geophys. Res. Lett. 30 (2003), doi:10.1029/2003GL018192.

[19] D. Angus, D. Wilson, E. Sandvol, J. Ni, Lithospheric structure of the Arabian and Eurasian collision zone in eastern Turkey from S-wave receiver functions, Geophys. J. Int. 166 (2006) 1335–1346.

[20] E.R. Engdahl, R.D. van der Hilst, R. Buland, Global teleseismic earthquake relocation with improved travel times and procedures for depth determination, Bull. Seismol. Soc. Am. 88 (1998) 722–743.

[21] J. VanDecar, R. Crosson, Determination of teleseismic relative phase arrival times using multi-channel cross-correlation and least squares, Bull. Seismol. Soc. Am. 80 (1990) 150–169.

[22] D. Zhao, Seismic structure and origin of hotspots and mantle plumes, Earth Planet. Sci. Lett. 192 (2001) 251–265.

[23] A.M. Dziewonski, F. Gilbert, The effect of small aspherical perturbation on travel times and a re-examiantion of the corrections for ellipticity, Geophys. J. R. Astron. Soc. 44 (1976) 7–17.

[24] D. Zhao, A. Hasegawa, S. Horiuchi, Tomographic imaging of P and S wave velocity structure beneath northeastern Japan, J. Geophys. Res. 97 (1992) 19909–19928.

[25] D. Zhao, J. Lei, Seismic ray path variations in a 3D global velocity model, Phys. Earth Planet. Inter. 141 (2004) 153–166.

[26] D. Zhao, A. Hasegawa, H. Kanamori, Deep structure of Japan subduction zones as derived from local, regional, and teleseismic events, J. Geophys. Res. 99 (1994) 22313–22329.

[27] J. Lei, D. Zhao, P-wave tomography and origin of the Changbai intraplate volcano in Northeast Asia, Tectonophysics 397 (2005) 281–295.

[28] J. Lei, D. Zhao, Teleseismic P-wave tomography and the upper mantle structure of the central Tien Shan, Phys. Earth Planet. Inter. (submitted for publication).

[29] C.C. Paige, M.A. Saunders, LSQR: an algorithm for spare linear equations and spare least squares, ACM Trans. Math. Softw. 8 (1982) 43–71.

[30] J. Lei, D. Zhao, Global P-wave tomography: on the effect of various mantle and core phases, Phys. Earth Planet. Inter. 154 (2006) 44–69.

[31] R. Allen, G. Nolet, W. Morgan, K. Vogfjord, B. Bergsson, P. Erlendsson, G. Foulger, S. Jakobsdottir, B. Julian, M. Pritchard, S. Ragnarsson, R. Stefansson, Imaging the mantle beneath Iceland using integrated seismological techniques, J. Geophys. Res. 107 (2002), doi:10.1029/2001JB000595.

[32] S. Hung, Y. Shen, L. Chiao, Imaging seismic velocity structure beneath the Iceland hot spot: a finite frequency approach, J. Geophys. Res. 109 (2004), doi:10.1029/2003JB002889.

[33] D. Zhao, J. Lei, T. Inoue, A. Yamada, S. Gao, Deep structure and origin of the Baikal refit zone, Earth Planet. Sci. Lett. 243 (2006) 681–691.

[34] J. Lei, H. Zhou, 3-D velocity structure of P-wave in the upper mantle beneath southeastern China and adjacent areas, Acta Seismol. Sin. 15 (2) (2002) 134–142.

[35] A. Maggi, K. Priestley, Surface waveform tomography of the Turkish–Iranian plateau, Geophys. J. Int. 160 (2005) 1068–1080.

[36] C. Piromallo, A. Morelli, P wave tomography of the mantle under the Alpine–Mediterranean area, J. Geophys. Res. 108 (2003), doi:10.1029/2002JB001757.

[37] J. Davies, F. von Blanckenburg, Slab breakoff: a model of lithosphere detachment and its test in the magmatism and deformation of collisional orogens, Earth Planet. Sci. Lett. 129 (1995) 85–102.

[38] I. Koulakov, S. Sobolev, A tomographic image of Indian lithosphere break-off beneath the Pamir–Hindukush region, Geophys. J. Int. 164 (2006) 425–440.

[39] M. Wortel, W. Spakman, Subduction and slab detachment in the Mediterranean–Carpathian region, Science 290 (2000) 1910–1917.

[40] C. Faccenna, O. Bellier, J. Martinod, C. Piromallo, V. Regard, Slab detachment beneath eastern Anatolian: a possible cause for the formation of the North Anatolian fault, Earth Planet. Sci. Lett. 242 (2006) 85–97.

[41] A. Rodgers, J. Ni, T. Hearn, Propagation characteristics of short-period Sn and Lg in the Middle East, Bull. Seismol. Soc. Am. 87 (1997) 396–413.

[42] F. Lemoine, et al., The NASA and DMA joint geopotential model, EOS, Trans. Am. Geophys. Union 77 (1996) 136 (Fall Meet. Suppl.).

[43] I. Aydin, H. Karat, A. Kocak, Curie-point depth map of Turkey, Geophys. J. Int. 162 (2005) 633–640.
[44] A. Tezcan, Geothermal explorations and heat flow in Turkey, in: M.L. Gupta, M. Yamamo (Eds.), Terrestrial Heat Flow and Geothermal Energy in Asia, Oxford and IBH Publishing Co. Pvt. Ltd., New Delhi, 1995, pp. 23–42.
[45] D. Zhao, Global tomographic images of mantle plumes and subducting slabs: insight into deep Earth dynamics, Phys. Earth Planet. Inter. 146 (2004) 3–34.
[46] M. Keskin, J. Pearce, J. Mitchell, Volcano-stratigraphy and geochemistry of collision-related volcanism on the Erzurum–Kars Plateau, northeastern Turkey, J. Volcanol. Geotherm. Res. 85 (1-4) (1998) 355–402.
[47] A. Sengor, S. Ozeren, T. Genc, E. Zor, East Anatolian high plateau as a mantle-supported, north–south shortened domal structure, Geophys. Res. Lett. 30 (2003), doi:10.1029/2003GL017858.
[48] M. Keskin, Magma generation by slab steepening and breakoff beneath a subduction–accretion complex: an alternative model for collision-related volcanism in Eastern Anatolia, Turkey, Geophys. Res. Lett. 30 (2003), doi:10.1029/2003GL01019.
[49] P. Wessel, W. Smith, New version of the Generic Mapping Tools (GMT) version 3.0 released, EOS Trans. AGU 76 (1995) 329.
[50] B.L.N. Kennett, E.R. Engdahl, Traveltimes for global earthquake location and phase identification, Geophys. J. Int. 105 (1991) 429–465.